Available on the CERN CDS information server **CMS PAS HIG-18-017**

CMS Physics Analysis Summary

Contact: cms-pag-conveners-higgs@cern.ch 2019/05/17

Search for lepton flavour violating decays of neutral heavy Higgs boson to $\mu\tau$ and eτ in proton-proton collisions at $\sqrt{s} = 13$ TeV

The CMS Collaboration

Abstract

A search for lepton flavor violating decays of a neutral heavy Higgs boson in the $\mu\tau$ and eτ decay modes is presented. The search is based on a dataset of 35.9 fb^{-1} proton-proton collisions collected with the CMS detector in 2016, at a center-of-mass energy of $\sqrt{s} = 13$ TeV. The tau leptons are reconstructed in the leptonic and hadronic decay modes. No signal is observed. The observed (expected) limits on the cross section times the branching fraction of a Higgs boson of mass in the range 200-900 GeV, decaying to $\mu\tau$ and eτ vary from 51.9 (57.4) fb to 1.6 (2.1) fb and from 94.1 (91.6) fb to 2.3 (2.3) fb, respectively.

1 Introduction

The discovery of the 125 GeV Higgs boson, H(125), at the CERN LHC in 2012 [1–3] was a major breakthrough in experimental particle physics. A combined study of 7 and 8 TeV data sets collected by the CMS and ATLAS collaborations shows the particle to have properties consistent with the standard model (SM) Higgs [4–9] including the spin, couplings and charge-parity (CP) assignment [10, 11]. Lepton flavour violating (LFV) decays of the H(125) are forbidden in the SM. However, despite its success, the SM is known to be incomplete and there exist many possible extensions of it that allow LFV decays of the H(125). These include the two Higgs doublet model [12], supersymmetric models [13–19], composite Higgs models [20, 21], models with flavour symmetries [22], Randall–Sundrum models [23–25], and others [26–34]. A common feature of many of these models is the presence of additional heavy neutral Higgs bosons (H and A) that would also have LFV decays [35].

The most recent search for LFV decays of the H(125) boson was performed by the CMS collaboration [36]. The search was performed in the $\mu\tau$ and $\mathrm{e}\tau$ channels using $35.9\,\mathrm{fb}^{-1}$ of proton-proton collision data, recorded at a center-of-mass energy of $\sqrt{s} = 13\,\mathrm{TeV}$. No signal was observed and the observed (expected) limits set on the branching fractions were $B(\mathrm{H}(125) \to \mu\tau) < 0.25\%(0.25\%)$ and to $B(\mathrm{H}(125) \to \mathrm{e}\tau) < 0.61\%(0.37\%)$ at the 95% confidence level. These constraints were a significant improvement over the previously set limits by the CMS and ATLAS collaborations using the $\sqrt{s} = 8\,\mathrm{TeV}$ proton-proton collision data set, corresponding to an integrated luminosity of about $20\,\mathrm{fb}^{-1}$ [37–40]. The previous CMS $\mathrm{H}(125) \to \mu\tau$ search, performed using 8 TeV proton-proton collision data, was reinterpreted as a search for high mass LFV H decays by a theory group [41]. Limits on the branching fraction times cross-section for the $\mathrm{H} \to \mu\tau$ channel were obtained for H mass (m_{H})$< 300\,\mathrm{GeV}$. This note describes the first direct search for LFV H decays for $m_{\mathrm{H}} < 900\,\mathrm{GeV}$. The search is performed in four decay channels, $\mathrm{H} \to \mu\tau_h$, $\mathrm{H} \to \mu\tau_{\mathrm{e}}$, $\mathrm{H} \to \mathrm{e}\tau_h$, $\mathrm{H} \to \mathrm{e}\tau_\mu$ where τ_h, τ_{e} and τ_μ correspond to the hadronic, electronic and muonic decay channels of τ leptons, respectively. The final state signatures are very similar to $\mathrm{H} \to \tau\tau$ decays, studied by CMS [42–45]and ATLAS [46]. However, there are some significant kinematic differences. The primary difference is that the muon (electron) in the LFV $\mathrm{H} \to \mu(\mathrm{e})\tau$ decay is produced promptly, and tends to have a higher momentum than in the $\mathrm{H} \to \tau_{\mu(\mathrm{e})}\tau$ decay. Also, there are fewer neutrinos in the LFV decay, all coming from the decay of the same tau lepton. This leads to the missing transverse momentum vector to be closely aligned with the visible decay products of the highly boosted tau lepton in the azimuthal plane. Only the gluon fusion production process is considered in this search and the signal is modelled assuming a narrow width of the Higgs boson. The search strategy is similar to the previous LFV H(125) searches performed by the CMS collaboration but optimized for higher mass Higgs boson decays.

This note is organized as follows. A brief overview of the CMS detector is given in section 2 followed by a description of the collision data and simulated samples used in the analysis in section 3 and the event reconstruction in section 4. The event selection is described in section 5 and the backgrounds are described in section 6. This is followed by a description of the systematic uncertainties in section 7. Finally, the results are presented in Section 8.

2 The CMS detector

A detailed description of the CMS detector, together with a definition of the coordinate system used and the relevant kinematic variables, can be found in Ref. [47]. The momenta of charged particles are measured with a silicon pixel and strip tracker that covers the pseudorapidity range $|\eta| < 2.5$, in a 3.8 T axial magnetic field. A lead tungstate crystal electromagnetic calorimeter (ECAL) and a brass and scintillator hadron calorimeter, both consisting of a barrel section and two endcaps, cover the pseudorapidity range $|\eta| < 3.0$. A steel and quartz-fibre Cherenkov forward detector extends the calorimetric coverage to $|\eta| < 5.0$. The outermost component of the CMS detector is the muon system, consisting of gas-ionization detectors placed in the steel flux-return yoke of the magnet to identify the muons traversing the detector. The two-level CMS trigger system selects events of interest for permanent storage. The first trigger level, composed of custom hardware processors, uses information from the calorimeters and muon detectors to select events in less than 3.2 μs. The software algorithms of the high-level trigger, executed on a farm of commercial processors, reduce the event rate to about 1 kHz using information from all detector subsystems.

3 Collision data and simulated events

The data used in this analysis is from proton-proton collisions at the LHC, at a center-of-mass energy of $\sqrt{s} = 13$ TeV, collected with the CMS detector, and corresponding to an integrated luminosity of 35.9 fb^{-1}. A trigger requiring a single muon is used to collect the data sample in the $\mathrm{H} \rightarrow \mu\tau$ channel. In the $\mathrm{H} \rightarrow \mathrm{e}\tau$ channel, triggers requiring a single electron or a combination of an electron and a muon are used depending on the final state. Simulated samples of signal and background events are produced with different event generators as follows. The $\mathrm{H} \rightarrow \mu\tau$ and $\mathrm{H} \rightarrow \mathrm{e}\tau$ decay samples are generated with POWHEG 2.0 [48–53]. Only the gluon fusion (ggH) [54] production mode has been considered. Samples are generated for a range of Higgs masses from 200 to 900 GeV. The Z + jets and W + jets processes are simulated using the MG5_aMC@NLO [55] generator at leading order (LO) with the MLM jet matching and merging [56]. The MG5_aMC@NLO generator is also used for diboson production which is simulated at next-to-LO (NLO) with the FxFx jet matching and merging [57]. POWHEG 2.0 and 1.0 are used for $\mathrm{t\bar{t}}$ and single top quark production, respectively. The POWHEG and MADGRAPH generators are interfaced with PYTHIA 8.212 [58] for parton showering, fragmentation, and decays. The PYTHIA parameters for the underlying event description are set to the CUETP8M1 tune [59]. Due to the high instantaneous luminosities attained during data taking, many events have multiple pp interactions per bunch crossing (pileup). The effect is taken into account in simulated samples, by generating concurrent minimum bias events. All simulated samples are weighted to match the pileup distribution observed in data, that has an average of approximately 27 interactions per bunch crossing. The CMS detector response is modelled using GEANT4 [60].

4 Event reconstruction

The global event reconstruction is performed using a particle-flow (PF) algorithm, which reconstructs and identifies each individual particle with an optimized combination of all subdetector information [61]. In this process, the identification of the particle type (photon, electron, muon, charged or neutral hadron) plays an important role in the determination of the particle direction and energy. The primary pp vertex of the event is identified as the reconstructed vertex with the largest value of summed physics-object p_{T}^2, where p_{T} is the transverse momentum. The physics objects are returned by a jet finding algorithm [62, 63] applied to all charged tracks associated with the vertex, plus the corresponding associated missing transverse momentum.

A muon is identified as a track in the silicon detectors, consistent with the primary pp vertex and with either a track or several hits in the muon system, associated with an energy deposit in the calorimeters compatible with the expectations for a muon [61, 64]. Identification is based on the number of spacial points measured in the tracker and in the muon system, the track quality and its consistency with the event vertex location. The energy is obtained from the corresponding track momentum.

An electron is identified as a charged particle track from the primary pp vertex in combination with one or more ECAL energy clusters. These clusters correspond to the track extrapolation to the ECAL and to possible bremsstrahlung photons emitted when interacting with the material of the tracker [65]. Electron candidates are accepted in the range $|\eta| < 2.5$, with the exception of the region $1.44 < |\eta| < 1.57$ where service infrastructure for the detector is located. They are identified using a multivariate (MVA) discriminator that combines observables sensitive to the amount of bremsstrahlung along the electron trajectory, the geometric and momentum matching between the electron trajectory and associated clusters, as well as various shower shape observables in the calorimeters. Electrons from photon conversions are removed. The energy of electrons is determined from a combination of the track momentum at the primary vertex, the corresponding ECAL cluster energy, and the energy sum of all bremsstrahlung photons attached to the track.

Charged hadrons are identified as charged particle tracks from the primary pp vertex neither reconstructed as electrons nor as muons. Neutral hadrons are identified as HCAL energy clusters not assigned to any charged hadron, or as ECAL and HCAL energy excesses with respect to the expected charged-hadron energy deposit. All the PF candidates are clustered into hadronic jets using the infrared and collinear safe anti-k_{T} algorithm [62], implemented in the FASTJET package [66], with a distance parameter of 0.4. The jet momentum is determined as the vector sum of all particle momenta in this jet, and is found in the simulation to be on average within 10% of the true momentum over the whole p_{T} spectrum and detector acceptance. An offset correction is applied to jet energies to take into account the contribution from pileup [67]. Jet energy corrections are derived from the simulation, and are confirmed with in situ measurements of the energy balance of dijet, multijet, photon + jet, and Z + jet events [68]. The variable $\Delta R = \sqrt{(\Delta\eta)^2 + (\Delta\phi)^2}$ is used to measure the separation between reconstructed objects in the detector. Any jet within $\Delta R = 0.4$ of the identified leptons is removed.

Hadronically decaying τ leptons are reconstructed and identified using the hadrons-plus-strips (HPS) algorithm [69, 70]. The reconstruction starts from a jet and searches for the products of the main τ lepton decay modes: one charged hadron and up to two neutral pions, or three charged hadrons. To improve the reconstruction efficiency in the case of conversion of the photons from neutral-pion decay, the algorithm considers the PF photons and electrons from a strip along the azimuthal direction ϕ. The charges of all the PF objects from tau lepton decay, except for the electrons from neutral pion candidates, are summed to reconstruct the tau lepton charge. An MVA discriminator, based on variables such as lifetime information, decay mode, multiplicity of neutral and charged particles in a cone around the reconstructed τ etc., is used to reduce the rate for quark- and gluon-initiated jets identified as τ candidates. The working point used in the analysis has an efficiency of about 50% for a genuine τ_h, with approximately a 0.2% misidentification rate for quark and gluon jets [70]. Additionally, muons and electrons misidentified as tau leptons are rejected using a dedicated set of selection criteria based on the consistency between the measurements in the tracker, calorimeters, and muon detectors. The specific identification criteria depend on the final state studied and on the background composition. The tau leptons that decay to muons and electrons are reconstructed as prompt muons and electrons as described above.

Jets misidentified as electrons and muons are suppressed by imposing isolation requirements.

The muon (electron) isolation is measured relative to its p_{T}^{ℓ} ($\ell = \mu, \mathrm{e}$) by summing over the p_{T} of PF particles in a cone with $\Delta R = 0.4$ (0.3) around the lepton:

$$I_{\mathrm{rel}}^{\ell} = \left(\sum p_{\mathrm{T}}^{\mathrm{charged}} + \max\left[0, \sum p_{\mathrm{T}}^{\mathrm{neutral}} + \sum p_{\mathrm{T}}^{\gamma} - p_{\mathrm{T}}^{\mathrm{PU}}\left(\ell\right)\right]\right) / p_{\mathrm{T}}^{\ell}.$$

where $p_{\mathrm{T}}^{\mathrm{charged}}$, $p_{\mathrm{T}}^{\mathrm{neutral}}$, and p_{T}^{γ} indicate the p_{T} of a charged particle, a neutral particle, and a photon within the cone, respectively. The neutral contribution to isolation from pileup, $p_{\mathrm{T}}^{\mathrm{PU}}\left(\ell\right)$, is estimated from the area of the jet and the average energy density of the event [71, 72] for the electron or from the sum of transverse momenta of charged hadrons not originating from the primary vertex scaled by a factor of 0.5 for the muons [64]. The charged contribution to isolation from pileup is rejected requiring the tracks to originate from the primary vertex.

All the reconstructed particles in the event are used to estimate the missing transverse momentum, $\vec{p}_{\mathrm{T}}^{\mathrm{miss}}$, which is defined as the negative of the vector $\vec{p}_{\mathrm{T}}$ sum of all identified PF objects in the event [73]. Its magnitude is referred to as $p_{\mathrm{T}}^{\mathrm{miss}}$.

The transverse mass $M_{\mathrm{T}}(\ell)$ is a variable formed from the lepton momentum and the missing transverse momentum vectors: $M_{\mathrm{T}}(\ell) = \sqrt{2|\vec{p}_{\mathrm{T}}^{\ell}||\vec{p}_{\mathrm{T}}^{\mathrm{miss}}|(1 - \cos\Delta\phi_{\ell - p_{\mathrm{T}}^{\mathrm{miss}}})}$, where $\Delta\phi_{\ell - p_{\mathrm{T}}^{\mathrm{miss}}}$ is the angle in the transverse plane between the lepton and the missing transverse momentum. The collinear mass, M_{col}, provides an estimate of m_{H} using the observed decay products of the Higgs boson candidate. It is reconstructed using the collinear approximation based on the observation that, since $m_{\mathrm{H}} \gg m_{\tau}$, the τ lepton decay products are highly Lorentz boosted in the direction of the τ candidate [74]. The neutrino momenta can be approximated to have the same direction as the other visible decay products of the τ ($\vec{\tau}^{\mathrm{vis}}$) and the component of the $\vec{p}_{\mathrm{T}}^{\mathrm{miss}}$ in the direction of the visible τ lepton decay products is used to estimate the transverse component of the neutrino momentum ($p_{\mathrm{T}}^{\nu,\mathrm{est}}$). The collinear mass can then be derived from the visible mass of the τ-μ or τ-e system, M_{vis}, as $M_{\mathrm{col}} = M_{\mathrm{vis}} / \sqrt{x_{\tau}^{\mathrm{vis}}}$, where x_{τ}^{vis} is the fraction of energy carried by the visible decay products of the τ, $x_{\tau}^{\mathrm{vis}} = p_{\mathrm{T}}^{\vec{\tau}^{\mathrm{vis}}} / (p_{\mathrm{T}}^{\vec{\tau}^{\mathrm{vis}}} + p_{\mathrm{T}}^{\nu,\mathrm{est}})$, and M_{vis} is the invariant mass of the visible decay products.

5 Event Selection

The event selection is made in two steps. A preliminary selection is followed by another final set of requirements on kinematic variables that exploit the distinct event topology of the signal. The event sample defined by the preliminary selection is used in the background estimation described in section 6. The preliminary selection is summarized in Table 1. It begins by requiring two isolated leptons of opposite charge, different flavour, and separated by $\Delta R > 0.3$. The isolation requirement for the τ_h candidates is included in the MVA used for the HPS identification algorithm described in Section 4. Events with additional e, μ, or τ_h candidates are vetoed. In addition, events with at least one jet arising from a b-quark as identified by the combined secondary vertex b-tagging algorithm [75] are vetoed.

The events are then divided into two categories according to the number of jets in the event. The jets are required to have $p_{\mathrm{T}} > 30$ GeV and $|\eta| < 4.7$. Events with no jets form the 0-jet category while events with one jet form the 1-jet category. The latter category enhances ggH production with initial state radiation and helps in increasing the sensitivity of the search. Events with more than one jet are discarded.

The final selection is given in Table 2. It begins by increasing the p_{T} requirement of the prompt lepton from the Higgs Boson decay as it provides a powerful discriminant against most back-

Table 1: Preliminary selection criteria applied to the kinematic variables for the $\mathrm{H} \to \mu\tau$ and $\mathrm{H} \to \mathrm{e}\tau$ analyses. The selected sample is used in the data-driven background estimation.

	$\mathrm{H} \to \mu\tau_{\mathrm{h}}$	$\mathrm{H} \to \mu\tau_{\mathrm{e}}$	$\mathrm{H} \to \mathrm{e}\tau_{\mathrm{h}}$	$\mathrm{H} \to \mathrm{e}\tau_{\mu}$
p_{T}^{μ}	$> 53\,\mathrm{GeV}$	$> 53\,\mathrm{GeV}$	–	> 10
$p_{\mathrm{T}}^{\mathrm{e}}$	–	$> 10\,\mathrm{GeV}$	$> 26\,\mathrm{GeV}$	$> 26\,\mathrm{GeV}$
p_{T}^{τ}	$> 30\,\mathrm{GeV}$	–	$> 30\,\mathrm{GeV}$	–
$\lvert\eta\rvert^{\mu}$	< 2.4	< 2.4	–	< 2.4
$\lvert\eta\rvert^{\mathrm{e}}$	–	< 2.4	< 2.1	< 2.4
$\lvert\eta\rvert^{\tau}$	< 2.3	–	< 2.3	–
$I_{\mathrm{rel}^{\mu}}$	–	< 0.15	–	< 0.15
$I_{\mathrm{rel}^{\mathrm{e}}}$	–	< 0.1	< 0.1	< 0.1
$\Delta R(\mu, \mathrm{e})$	–	< 0.3	–	< 0.3
$\Delta R(\mu, \tau)$	< 0.3	–	–	–
$\Delta R(\mathrm{e}, \tau)$	–	–	< 0.3	–

grounds. The associated τ lepton in the decay is highly Lorentz boosted leading to a collimation of the decay products. This can be exploited by either limiting the azimuthal separation of the decay products including the $\vec{p}_{\mathrm{T}}$ that arises from the neutrino or imposing a requirement on the transverse mass ($M_{\mathrm{T}}(\tau, p_{\mathrm{T}}^{\mathrm{miss}})$ which is strongly correlated with the azimuthal separation. These selection criteria are optimized for each decay mode in two m_{H} ranges to obtain the most stringent expected limits. The low mass and high mass regions are defined to be $200 < m_{\mathrm{H}} < 450\,\mathrm{GeV}$ and $450 < m_{\mathrm{H}} < 900\,\mathrm{GeV}$, respectively. A binned likelihood is then used to fit the M_{col} distributions for the signal and the background contributions.

6 Background Estimation

The most significant background in the $\mu\tau_{\mathrm{h}}$ and $\mathrm{e}\tau_{\mathrm{h}}$ channels comes from the $\mathrm{W}+\mathrm{jets}$ process and from events comprised uniquely of jets produced through the strong interaction, referred to as quantum chromodynamics (QCD) multijet events. In these processes, jets are misidentified as leptons. This background is estimated with collision data. Top quark-antiquark production is the main background in the $\mu\tau_{\mathrm{e}}$ and $\mathrm{e}\tau_{\mu}$ channels. It is estimated using simulated data. Other smaller backgrounds include electroweak diboson (WW, WZ and ZZ), $\mathrm{Z} \to \ell\ell$ ($\ell = \mathrm{e}, \mu, \tau$) $+\,\mathrm{jets}$, SM Higgs boson production ($\mathrm{H} \to \tau\tau, \mathrm{WW}$), $\mathrm{W}\gamma^{(*)} +\mathrm{jets}$, and single top quark production processes. These are also estimated using simulated data. Gluon fusion and associated production mechanisms are considered for the SM Higgs background. The background estimation techniques are described in detail below. The background estimation is validated with control samples that are enhanced with the dominant backgrounds.

The $\mathrm{Z} \to \ell\ell$ background is estimated with simulated data samples. A reweighting is applied to the the generator-level Z p_{T} and $m_{\ell\ell}$ distributions to correct for a shape discrepancy between collision and simulation data. The reweighting factors, extracted from a $Z \to \mu\mu$ control region, are applied in bins of Z p_{T} and $m_{\ell\ell}$. Corrections for $e \to \tau_h$ and $\mu \to \tau_h$ misidentification rates are applied when the reconstructed τ_h candidate is matched to an electron or a muon, respectively, at the generator level. These corrections depend on the lepton η and are measured in $Z \to \ell\ell$ data events. The $\mathrm{t\bar{t}}$ background is estimated using simulated data. The estimate in the signal region is corrected based on factors derived from a control region enriched in $\mathrm{t\bar{t}}$ events. This is selected by requiring the preliminary selection with the additional requirement that at least one of the jets is a b-tagged jet. Figure 1 (top left) shows the data compared to the

Table 2: Final event selection criteria for the low mass range, $200 < m_{\mathrm{H}} < 450\,\mathrm{GeV}$, and the high mass range, $450 < m_{\mathrm{H}} < 900\,\mathrm{GeV}$, investigated in the $\mathrm{H} \to \mu\tau$ and $\mathrm{H} \to \mathrm{e}\tau$ analyses.

	Low mass range	High mass range
$\mathrm{H} \to \mu\tau_{\mathrm{h}}$		
0-jet	$p_{\mathrm{T}}^{\mu} > 60$ GeV, $p_{\mathrm{T}}^{\tau} > 30$ GeV $M_T(\tau) < 105$ GeV	$p_{\mathrm{T}}^{\mu} > 150$ GeV, $p_{\mathrm{T}}^{\tau} > 45$ GeV $M_T(\tau) < 200$ GeV
1-jet	$p_{\mathrm{T}}^{\mu} > 60$ GeV, $p_{\mathrm{T}}^{\tau} > 30$ GeV $M_T(\tau) < 120$ GeV	$p_{\mathrm{T}}^{\mu} > 150$ GeV, $p_{\mathrm{T}}^{\tau} > 45$ GeV $M_T(\tau) < 230$ GeV
$\mathrm{H} \to \mu\tau_{\mathrm{e}}$		
0-jet	$p_{\mathrm{T}}^{\mu} > 60$ GeV, $p_{\mathrm{T}}^{\mathrm{e}} > 10$ GeV $\Delta\phi(\mathrm{e}, \vec{p}_{\mathrm{T}}^{\mathrm{miss}}) < 0.7$ $\Delta\phi(\mathrm{e}, \mu) > 2.2$	$p_{\mathrm{T}}^{\mu} > 150$ GeV, $p_{\mathrm{T}}^{\mathrm{e}} > 10$ GeV $\Delta\phi(\mathrm{e}, \vec{p}_{\mathrm{T}}^{\mathrm{miss}}) < 0.3$ $\Delta\phi(\mathrm{e}, \mu) > 2.2$
1-jet	$p_{\mathrm{T}}^{\mu} > 60$ GeV, $p_{\mathrm{T}}^{\mathrm{e}} > 10$ GeV $\Delta\phi(\mathrm{e}, \vec{p}_{\mathrm{T}}^{\mathrm{miss}}) < 0.7$ $\Delta\phi(\mathrm{e}, \mu) > 2.2$	$p_{\mathrm{T}}^{\mu} > 150$ GeV, $p_{\mathrm{T}}^{\mathrm{e}} > 10$ GeV $\Delta\phi(\mathrm{e}, \vec{p}_{\mathrm{T}}^{\mathrm{miss}}) < 0.3$ $\Delta\phi(\mathrm{e}, \mu) > 2.2$
$\mathrm{H} \to \mathrm{e}\tau_{\mathrm{h}}$		
0-jet	$p_{\mathrm{T}}^{\mathrm{e}} > 60$ GeV, $p_{\mathrm{T}}^{\tau} > 30$ GeV $M_T(\tau) < 105$ GeV	$p_{\mathrm{T}}^{\mathrm{e}} > 150$ GeV, $p_{\mathrm{T}}^{\tau} > 45$ GeV $M_T(\tau) < 200$ GeV
1-jet	$p_{\mathrm{T}}^{\mathrm{e}} > 60$ GeV, $p_{\mathrm{T}}^{\tau} > 30$ GeV $M_T(\tau) < 120$ GeV	$p_{\mathrm{T}}^{\mathrm{e}} > 150$ GeV, $p_{\mathrm{T}}^{\tau} > 45$ GeV $M_T(\tau) < 230$ GeV
$\mathrm{H} \to \mathrm{e}\tau_{\mu}$		
0-jet	$p_{\mathrm{T}}^{\mathrm{e}} > 60$ GeV, $p_{\mathrm{T}}^{\mu} > 10$ GeV $\Delta\phi(\mu, \vec{p}_{\mathrm{T}}^{\mathrm{miss}}) < 0.7$ $\Delta\phi(\mathrm{e}, \mu) > 2.2$	$p_{\mathrm{T}}^{\mathrm{e}} > 150$ GeV, $p_{\mathrm{T}}^{\mu} > 10$ GeV $\Delta\phi(\mu, \vec{p}_{\mathrm{T}}^{\mathrm{miss}}) < 0.3$ $\Delta\phi(\mathrm{e}, \mu) > 2.2$
1-jet	$p_{\mathrm{T}}^{\mathrm{e}} > 60$ GeV, $p_{\mathrm{T}}^{\mu} > 10$ GeV $\Delta\phi(\mu, \vec{p}_{\mathrm{T}}^{\mathrm{miss}}) < 0.7$ $\Delta\phi(\mathrm{e}, \mu) > 2.2$	$p_{\mathrm{T}}^{\mathrm{e}} > 150$ GeV, $p_{\mathrm{T}}^{\mu} > 10$ GeV $\Delta\phi(\mu, \vec{p}_{\mathrm{T}}^{\mathrm{miss}}) < 0.3$ $\Delta\phi(\mathrm{e}, \mu) > 2.2$

background estimate in the $t\bar{t}$ enriched region in the $\mathrm{H} \rightarrow \mu\tau_{\mathrm{e}}$ channel.

Jets misidentified as leptons are a source of background that comes from $\mathrm{W}+\text{jets}$ and QCD multijet events. In $\mathrm{W}+\text{jets}$ events, one lepton candidate is a real lepton from the W decay and the other is a jet misidentified as a lepton. In QCD multijet events both lepton candidates are misidentified jets. A fully data driven technique is used to estimate the misidentified lepton background in the $\mu\tau_{\mathrm{h}}$ and $\mathrm{e}\tau_{\mathrm{h}}$ channels in which it is the dominant contribution. In the $\mu\tau_{\mathrm{e}}$ and $\mathrm{e}\tau_{\mu}$ channels, this background is estimated using a semi data-driven technique (previously used in [36] and [44]) in which the misidentified $\mathrm{W}+\text{jets}$ background is estimated from simulation and the QCD background with data, as the reduced size of the sample limits the fully data-driven technique.

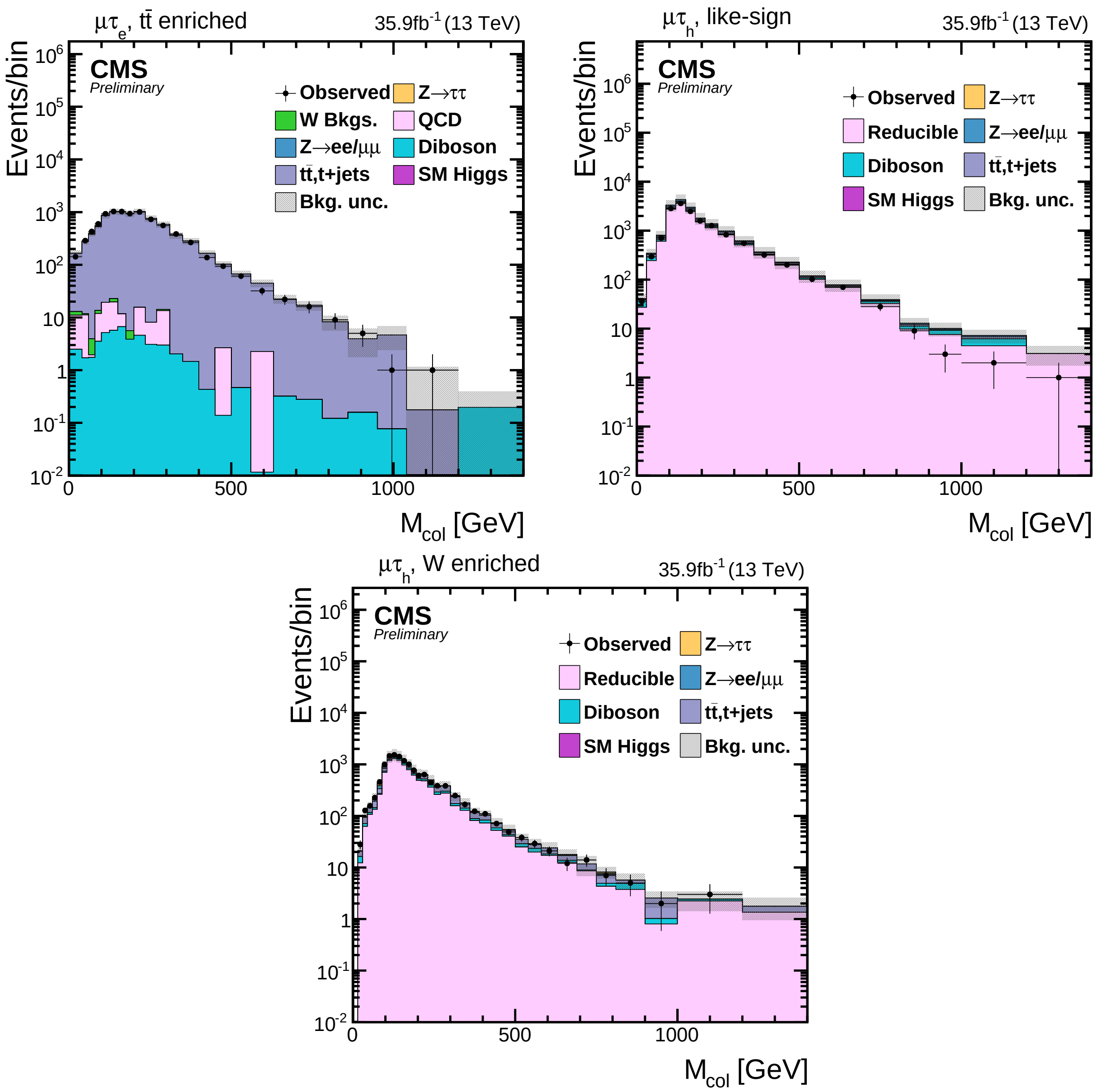

Figure 1: The M_{col} distribution in the $\mathrm{t}\bar{\mathrm{t}}$ enriched (top left), like-sign lepton (top right), and $\mathrm{W}+\text{jets}$ enriched (bottom) control samples defined in the text. The distributions include both statistical and systematic uncertainties.

Fully data-driven technique

The misidentified lepton background is estimated from collision data samples. The misidentification probabilities, f_i where $i = \mathrm{e}, \mu$ or τ_h, are evaluated with independent $\mathrm{Z} + \text{jets}$ data sets and then applied to a control sample. The control sample is obtained by relaxing the signal selection requirements, typically isolation, and excluding events passing the signal selection. The f_i are estimated using events with a Z boson candidate plus one jet that can be misidentified as a lepton. The Z boson candidate is formed requiring two muons with $p_{\mathrm{T}} > 26$ GeV, $|\eta| < 2.4$, and $I^{\ell}_{\mathrm{rel}} < 0.15$ (0.25). The muons are required to have opposite charge and their invariant mass, $m_{\mu\mu}$, must satisfy $76 < m_{\mu\mu} < 106\,\mathrm{GeV}$. The contribution from diboson events, where the third lepton candidate corresponds to a genuine lepton, is subtracted using simulated data. Two $\mathrm{Z} + \text{jets}$ samples are defined: a signal-like one, in which the jet satisfies the same lepton selection criteria used in the $\mathrm{H} \to \mathrm{e}\tau$ or $\mathrm{H} \to \mu\tau$ selections, and a background-enriched $\mathrm{Z} + \text{jets}$ sample with relaxed lepton identification on the jet but excluding events selected in the signal-like sample. The requirements for the third lepton candidate depend on the lepton flavour. The two samples are used to estimate f_i as

$$f_i = \frac{N_i(\mathrm{Z} + \text{jets signal-like})}{N_i(\mathrm{Z} + \text{jets background-enriched}) + N_i(\mathrm{Z} + \text{jets signal-like})},$$

where $N_i(\mathrm{Z} + \text{jets signal-like})$ is the number of events with a third lepton candidate that passes the signal-like sample selection, and $N_i(\mathrm{Z} + \text{jets background-enriched})$ is the number of events in the background-enriched sample. The background-enriched lepton selection used to estimate the misidentified μ and e contribution requires an isolation of $0.15 < I^{\ell}_{\mathrm{rel}} < 0.25$ and $0.1 < I^{\ell}_{\mathrm{rel}} < 0.5$, respectively. In both cases the misidentification rate is computed and applied as a function of the lepton p_{T}. The lepton selection for the τ_h background-enriched sample requires that the tau candidates are identified using a loose HPS working point but are not identified by the tight working point used for the signal selection. The loose and the tight working points have an efficiency of 75% and 60% for genuine τ_h candidates, respectively. The misidentification rates have a p_{T} dependence that varies with the number of charged pions in the decay. They are estimated and applied as a function of p_{T} and for either one charged pion or more than one charged pion in the decay. The misidentified lepton background in the signal sample is obtained from control samples for each lepton flavour. The selection requirements for these samples are the same as for the signal sample except that the lepton passes the identification and isolation criteria used for the $\mathrm{Z} + \text{jets}$ background-enriched sample but not those defining the $\mathrm{Z} + \text{jets}$ signal-like sample. Each event is weighted by a factor $f_i/(1 - f_i)$. The background from misidentified electrons and muons is estimated to be less than 5% of the misidentified tau lepton background and is neglected.

The background estimate is validated in a like-sign sample applying the misidentification rate f_i to events selected by inverting the charge requirement of the lepton pair in both the background-enriched and the signal-like samples. It is performed after the preliminary selection described in Section 5. Figure 1 (top right) shows the data compared to the background estimate in the like-sign control region for the $\mathrm{H} \to \mu\tau_{\mathrm{h}}$ channel. The like-sign selection enhances the misidentified lepton background and this sample is expected to be composed of a similar fraction of $\mathrm{W} + \text{jets}$ and QCD multijet events. The background estimate is also validated in a W boson enriched control sample. This data sample is obtained by applying the signal sample requirements and $50 < M_{\mathrm{T}}(\ell) < 110\,\mathrm{GeV}$ ($\ell = \mathrm{e}$ or μ) and $M_{\mathrm{T}}(\tau_h) > 50\,\mathrm{GeV}$. The misidentified lepton background in the signal region and W boson enriched control sample are both dominated by $\mathrm{W} + \text{jets}$ events with QCD multijet events forming a small fraction of the samples. Figure 1 (bottom) shows the data compared to the background estimate in the W enriched sample for the $\mathrm{H} \to \mu\tau_\mathrm{h}$ channel. The background estimate for the $\mathrm{H} \to \mathrm{e}\tau_\mathrm{h}$ channel is also validated with the same samples and gives similar agreement.

Semi data-driven technique

The $\mathrm{W}+\text{jets}$ background contribution to the misidentified-lepton background is estimated with simulated data samples. The QCD multijet contribution is estimated with like-sign collision data events that pass the signal requirement. The expected yield from non-QCD processes is subtracted using simulated data. The resulting sample is then rescaled to account for the differences between the composition in the like- and opposite-sign samples. The scaling factors are extracted from QCD multijet enriched control samples, composed of events with the lepton candidates satisfying inverted isolation requirements as illustrated in Ref. [44]. This technique is chosen for the leptonically decaying tau channels as larger event yields gives a more precise background estimation.

7 Systematic uncertainties

Systematic uncertainties arise from both experimental and theoretical sources and affect the normalization or the shape of the collinear mass distribution. They are summarized in Table 3. The uncertainties in the lepton (e, μ, τ_h) selection including the trigger, identification, and isolation efficiencies are estimated using tag-and-probe measurements in collision datasets of Z bosons decaying to $\mathrm{ee}, \mu\mu, \tau_\mu\tau_h$ [64, 65, 70]. The b tagging efficiency is measured in collision data and the event simulation is corrected accordingly with the measurement uncertainty as the systematic error. The uncertainties on the $\mathrm{Z} \to \mathrm{ee}, \mu\mu, \tau\tau$, WW, ZZ, $\mathrm{W}\gamma$, $t\bar{t}$ and single top production background contributions arise predominantly from the measured cross sections of these processes. Shape and normalization uncertainties arising from the uncertainty in the jet energy scale are computed by propagating, to the fit templates of each process, the effect of altering each source of jet energy scale uncertainty by $\pm 1\sigma$. There are 27 independent sources of jet energy scale uncertainty, fully correlated between categories and τ decay channels. The uncertainty on the τ_h energy scale is treated independently for $\mathrm{H} \to \mu\tau$ and $\mathrm{H} \to \mathrm{e}\tau$. It is propagated to the collinear mass distributions. The uncertainties in the estimate of the misidentified-lepton backgrounds ($\mu \to \tau_h$, $\mathrm{e} \to \tau_h$, jet $\to \tau_h, \mu, \mathrm{e}$) are extracted from the validation tests in control samples, described in Section 6. The uncertainty in the energy scale of electrons and muons misidentified as taus is propagated to the M_{col} distributions. Systematic uncertainties on the electron energy scale and resolution include the effects of electron selection efficiency, pseudorapidity dependence, and categorization summed in quadrature. The resolution systematics have negligible effect. There is also an uncertainty in the unclustered energy scale. The unclustered energy comes from jets below 10 GeV and PF candidates not within jets. It is also propagated to $E_{\mathrm{T}}^{\mathrm{miss}}$. The unclustered energy scale is considered independently for charged particles, photons, neutral hadrons, and very forward particles which are not contained in jets. The effect of shifting the energy of each particle by its uncertainty leads to both changes in shape of the distribution and in the yield. The four different systematic uncertainties are considered uncorrelated. The uncertainties in the Higgs boson production cross sections due to the factorization and the renormalization scales, as well as the parton distribution functions (PDF) and the strong coupling constant (α_s), result in changes in normalization. They are taken from Ref. [76] and summarized in Table 3 and Table 4. Only effects on the total rate are considered. Effects on acceptance have been neglected.

The bin-by-bin uncertainties account for the statistical uncertainties in every bin of the template distributions of every process, and are uncorrelated between bins, processes, and categories.

Table 3: The systematic uncertainties for the four channels. All uncertainties are treated as correlated between the categories, except those with two or more values separated by the $\oplus$ symbol. In the case of two values, the first value is the correlated uncertainty and the second value is the uncorrelated uncertainty for each individual category. In the case of three values, the first and second values correspond to uncertainties arising from QCD scale and PDF variations while the third value is the uncorrelated uncertainty for each individual category. Two values separated by the – sign represent the range of the uncertainties from the different sources and/or in the different jet categories.

Systematic uncertainty	$\mathrm{H} \to \mu\tau_h$	$\mathrm{H} \to \mu\tau_\mathrm{e}$	$\mathrm{H} \to \mathrm{e}\tau_h$	$\mathrm{H} \to \mathrm{e}\tau_\mu$
Muon trigger/ID/isolation	2%	2%	—	2%
Electron trigger/ID/isolation	—	2%	2%	2%
Hadronic τ efficiency	5%	—	5%	—
High p_T τ efficiency	$^{+5}_{-35}\% \times p_\mathrm{T}/$ TeV	—	$^{+5}_{-35}\% \times p_\mathrm{T}/$ TeV	—
b tagging veto	2.0–2.5%	2.0–2.5%	2.0–2.5%	2.0–2.5%
$\mathrm{Z} \to \mu\mu/ee +$ jets background	—	0.1%$\oplus$2%$\oplus$5%	—	0.1%$\oplus$2%$\oplus$5%
$\mathrm{Z} \to \tau\tau +$ jets background	0.1%$\oplus$2%$\oplus$5%	0.1%$\oplus$2%$\oplus$5%	0.1%$\oplus$2%$\oplus$5%	0.1%$\oplus$2%$\oplus$5%
$\mathrm{W} +$ jets background	—	0.8%$\oplus$3.8%$\oplus$5%	—	0.8%$\oplus$3.8%$\oplus$5%
WW, ZZ, WZ background	3.5%$\oplus$5%$\oplus$5%	3.5%$\oplus$5%$\oplus$5%	3.5%$\oplus$5%$\oplus$5%	3.5%$\oplus$5%$\oplus$5%
$\mathrm{W} + \gamma$ background	—	10%$\oplus$5%	—	10%$\oplus$5%
Single top quark background	3%$\oplus$5%$\oplus$5%	3%$\oplus$5%$\oplus$5%	3%$\oplus$5%$\oplus$5%	3%$\oplus$5%$\oplus$5%
$\mathrm{t\bar{t}}$ background	10%$\oplus$5%	10%$\oplus$5%	10%$\oplus$5%	10%$\oplus$5%
SM Higgs Renorm./fact. scales	3.9 %	3.9 %	3.9 %	3.9 %
SM Higgs PDF+α_s	3.2 %	3.2 %	3.2 %	3.2 %
QCD multijet background	—	30%	—	30%
$\mu \to \tau_h$ background	25%	—	—	—
$\mathrm{e} \to \tau_h$ background	—	—	12%	—
jet $\to \tau_h$ background	30%$\oplus$10%	—	30%$\oplus$10%	—
Jet energy scale	3–20%	3–20%	3-20%	3–20%
τ_h energy scale	1.2%	—	1.2%	—
$\mu, \mathrm{e} \to \tau_h$ energy scale	1.5%	—	3%	—
e energy scale	—	0.1-0.5%	0.1-0.5%	0.1-0.5%
μ energy scale	0.2%	0.2%	-	0.2%
Unclustered energy scale	$\pm1\sigma$	$\pm1\sigma$	$\pm1\sigma$	$\pm1\sigma$
Integrated Luminosity	2.5%	2.5%	2.5%	2.5%

Table 4: Theoretical uncertainties applied to the Higgs boson production cross sections for the different masses.

m_H (GeV)	Cross Section (pb)	TH Gaussian %	$\pm$(PDF+α_s) %
200.00	16.94	$\pm$1.8	$\pm$3.0
300.00	6.59	$\pm$1.8	$\pm$3.0
450.00	2.30	$\pm$2.0	$\pm$3.1
600.00	1.00	$\pm$2.1	$\pm$3.5
750.00	0.50	$\pm$2.1	$\pm$4.0
900.00	0.27	$\pm$2.2	$\pm$4.6

Shape uncertainties related to the pileup have been considered by varying the minimum bias cross section in the computation of the pileup events in data by 5%. The new values are then used to compute the weights for the simulated samples and these are applied, event by event, to produced alternative collinear mass distributions used as shape uncertainties in the fit. The uncertainty on the integrated luminosity affects all processes with normalization taken directly from simulation. Other minimum bias event modelling and simulation uncertainties are estimated to be much smaller than those on the rate and are therefore neglected.

8 Results

After all selection criteria have been applied, a maximum likelihood fit is performed on the M_{col} for signal and background. Each systematic uncertainty is used as a nuisance parameter in the fit. No significant excess is observed in any category. The fits are performed per channel and category, and then combined to set 95% CL upper limits on heavy Higgs boson production cross section times branching ratio to LFV lepton pairs, $\sigma(gg \to \mathrm{H}) \times \mathcal{B}(\mathrm{H} \to \mu\tau)$ and $\sigma(gg \to \mathrm{H}) \times \mathcal{B}(\mathrm{H} \to \mathrm{e}\tau)$. The limits are set for a set of discrete values of m_{H} in the range investigated. Limits for intermediate points of the mass range in steps of 50 GeV are also extracted where simulated samples are not available. This is done by linear interpolation of the available signals shapes to a particular mass point to obtain a template which is then used in the limit estimation. A profiled likelihood method is used to derive all results assuming the asymptotic approximation [77], and to set upper bounds on the branching fraction the $\mathrm{CL_s}$ method [78, 79] is used.

8.1 $\mathrm{H} \to \mu\tau$ results

The distributions of the collinear mass M_{col} compared to the fitted signal and background contributions in the $\mathrm{H} \to \mu\tau_{\mathrm{h}}$ and $\mathrm{H} \to \mu\tau_{\mathrm{e}}$ channel, in each jet category, are shown in Figs. 2 and 3. No excess over the background expectation is observed. The observed and median expected 95% CL upper limits on $\sigma(gg \to \mathrm{H}) \times \mathcal{B}(\mathrm{H} \to \mu\tau)$ are given for each category in Table 5. The limits are also summarized graphically in Fig. 4, for the individual categories, and in Fig. 5, for the combination of both categories.

8.2 $\mathrm{H} \to \mathrm{e}\tau$ results

The distributions of the collinear mass M_{col} compared to the fitted signal and background contributions in the $\mathrm{H} \to \mathrm{e}\tau_{\mathrm{h}}$ and $\mathrm{H} \to \mathrm{e}\tau_{\mu}$ channel, in each category, are shown in Figs. 6 and 7. No excess over the background expectation is observed. The observed and median expected 95% CL upper limits on $\sigma(gg \to \mathrm{H}) \times \mathcal{B}(\mathrm{H} \to \mathrm{e}\tau)$)are given for each category in Table 6. The limits are also summarized graphically in Fig. 8, for the individual categories, and Fig. 9, for the combination of both categories.

9 Summary

This note presents the first direct search for LFV decays of a heavy neutral Higgs boson in the $\mu\tau$ and $\mathrm{e}\tau$ channels. The dataset analyzed corresponds to an integrated luminosity of $35.9\,\mathrm{fb}^{-1}$ of proton-proton collision data recorded at $\sqrt{s} = 13\,\mathrm{TeV}$. The results are extracted by a fit to M_{col} distributions. No evidence is found for lepton flavor violating decays of a heavy Higgs boson in the investigated mass range. The observed (expected) limits on the cross section times the branching fraction of a heavy Higgs boson of mass in the range 200-900 GeV, decaying to $\mu\tau$ and $\mathrm{e}\tau$ vary from 51.9 (57.4) fb to 1.6 (2.1) fb and from 97.4 (91.6) fb to 2.3 (2.3) fb respectively.

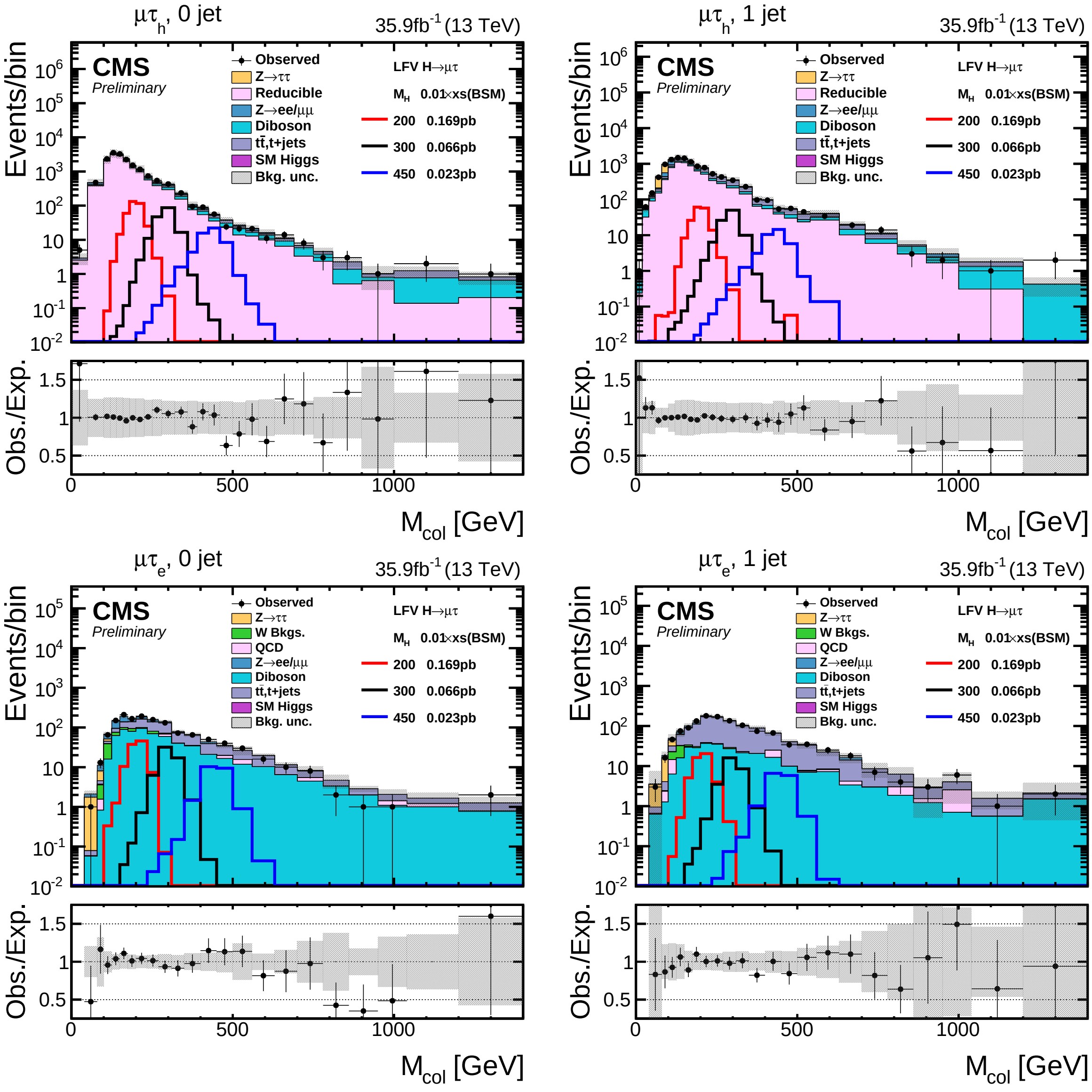

Figure 2: The M_{col} distribution in the signal region, for the $\mu\tau_h$ (top) and $\mu\tau_e$ (bottom) channels for the Higgs mass in the range 200-450 GeV for 0-jet (left) and 1-jet (right) categories.

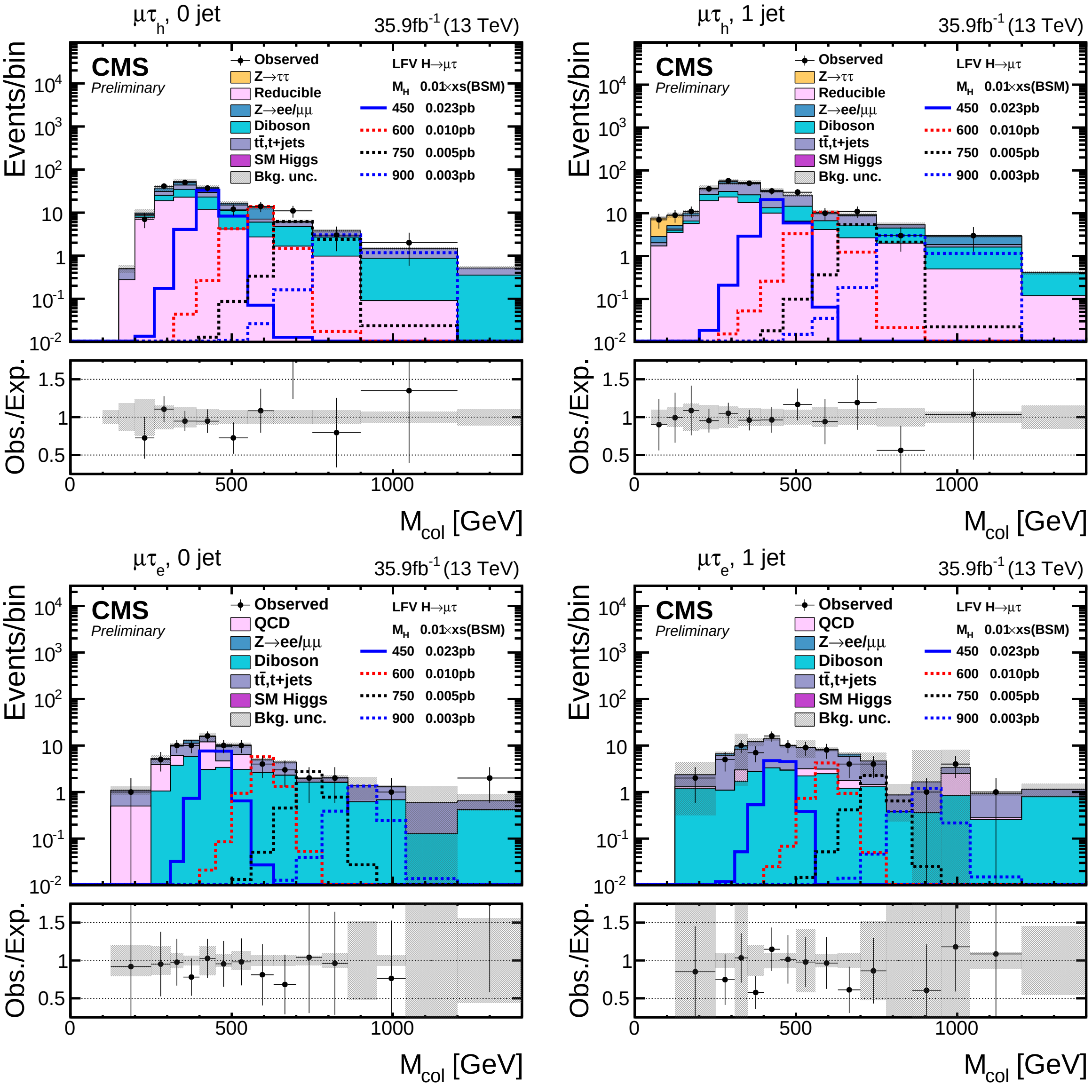

Figure 3: The M_{col} distribution in the signal region, for the $\mu\tau_h$ (top) and $\mu\tau_e$ (bottom) channels for the Higgs mass in the range 450-900 GeV for 0-jet (left) and 1-jet (right) categories.

Table 5: The observed and median expected 95% limits on $\sigma(gg \to \mathrm{H}) \times B(\mathrm{H} \to \mu\tau)$.

Median expected 95% C.L. limit on $\sigma(gg \to \mathrm{H}) \times B(\mathrm{H} \to \mu\tau)$ (fb)

	$\mu\tau_{\mathrm{e}}$			$\mu\tau_h$			$\mu\tau$		
	0 jet	1 jet	comb	0 jet	1 jet	comb	0 jet	1 jet	comb
200	107.5	209.8	95.6	79.7	151.6	72.5	63.7	126.1	57.4
300	49.8	108.6	45.2	31.0	54.8	27.7	25.9	48.8	23.4
450	17.5	32.8	20.4	9.4	15.3	8.0	8.2	13.6	7.7
600	10.4	17.9	8.9	6.2	8.3	4.9	5.1	7.4	4.2
750	8.0	18.2	6.1	4.3	5.4	3.1	3.6	4.7	2.7
900	6.9	15.4	4.9	3.3	4.3	2.4	2.8	3.5	2.1

Observed 95% C.L. limit on $\sigma(gg \to \mathrm{H}) \times B(\mathrm{H} \to \mu\tau)$ (fb)

	$\mu\tau_{\mathrm{e}}$			$\mu\tau_h$			$\mu\tau$		
	0 jet	1 jet	comb	0 jet	1 jet	comb	0 jet	1 jet	comb
200	147.8	262.1	159.4	53.1	136.9	46.4	53.3	133.9	51.9
300	30.1	100.8	29.3	67.6	49.4	51.4	33.2	45.5	32.7
450	31.1	35.3	23.7	9.1	14.2	7.3	14.7	14.6	8.1
600	8.1	15.2	6.8	7.5	7.4	5.3	9.1	7.4	4.1
750	6.5	7.8	4.7	4.8	4.8	3.2	3.6	4.7	2.5
900	4.4	5.6	2.9	4.6	2.6	2.3	3.0	3.5	1.6

Table 6: The observed and median expected 95% limits on $\sigma(gg \to \mathrm{H}) \times B(\mathrm{H} \to \mathrm{e}\tau)$.

Median expected 95% C.L. limit on $\sigma(gg \to \mathrm{H}) \times B(\mathrm{H} \to \mathrm{e}\tau)$ (fb)

	$\mathrm{e}\tau_\mu$			$\mathrm{e}\tau_h$			$\mathrm{e}\tau$		
	0 jet	1 jet	comb	0 jet	1 jet	comb	0 jet	1 jet	comb
200	158.2	366.6	142.3	135.7	238.9	120.1	102.9	200.5	91.6
300	57.9	123.0	52.3	42.9	70.3	37.5	34.5	62.0	30.2
450	20.4	32.6	17.2	10.1	18.0	8.7	9.0	15.4	7.8
600	17.4	22.1	11.9	8.6	11.6	6.8	7.5	9.9	5.9
750	8.6	10.5	6.2	4.9	6.5	3.7	4.1	5.3	3.0
900	8.5	9.0	5.7	4.0	4.7	2.6	3.3	4.0	2.3

Observed 95% C.L. limit on $\sigma(gg \to \mathrm{H}) \times B(\mathrm{H} \to \mathrm{e}\tau)$ (fb)

	$\mathrm{e}\tau_\mu$			$\mathrm{e}\tau_h$			$\mathrm{e}\tau$		
	0 jet	1 jet	comb	0 jet	1 jet	comb	0 jet	1 jet	comb
200	119.2	365.3	117.8	179.4	197.8	139.6	103.2	180.1	94.1
300	85.1	208.7	94.5	56.4	56.4	43.2	50.6	65.4	46.0
450	14.0	25.1	11.7	7.6	16.9	6.8	5.9	13.2	5.2
600	17.4	15.1	11.7	9.3	9.1	6.3	8.8	6.9	5.8
750	5.1	9.5	4.1	4.7	5.6	3.3	2.9	4.5	2.3
900	7.7	8.3	5.3	3.8	5.0	2.7	3.1	4.0	2.3

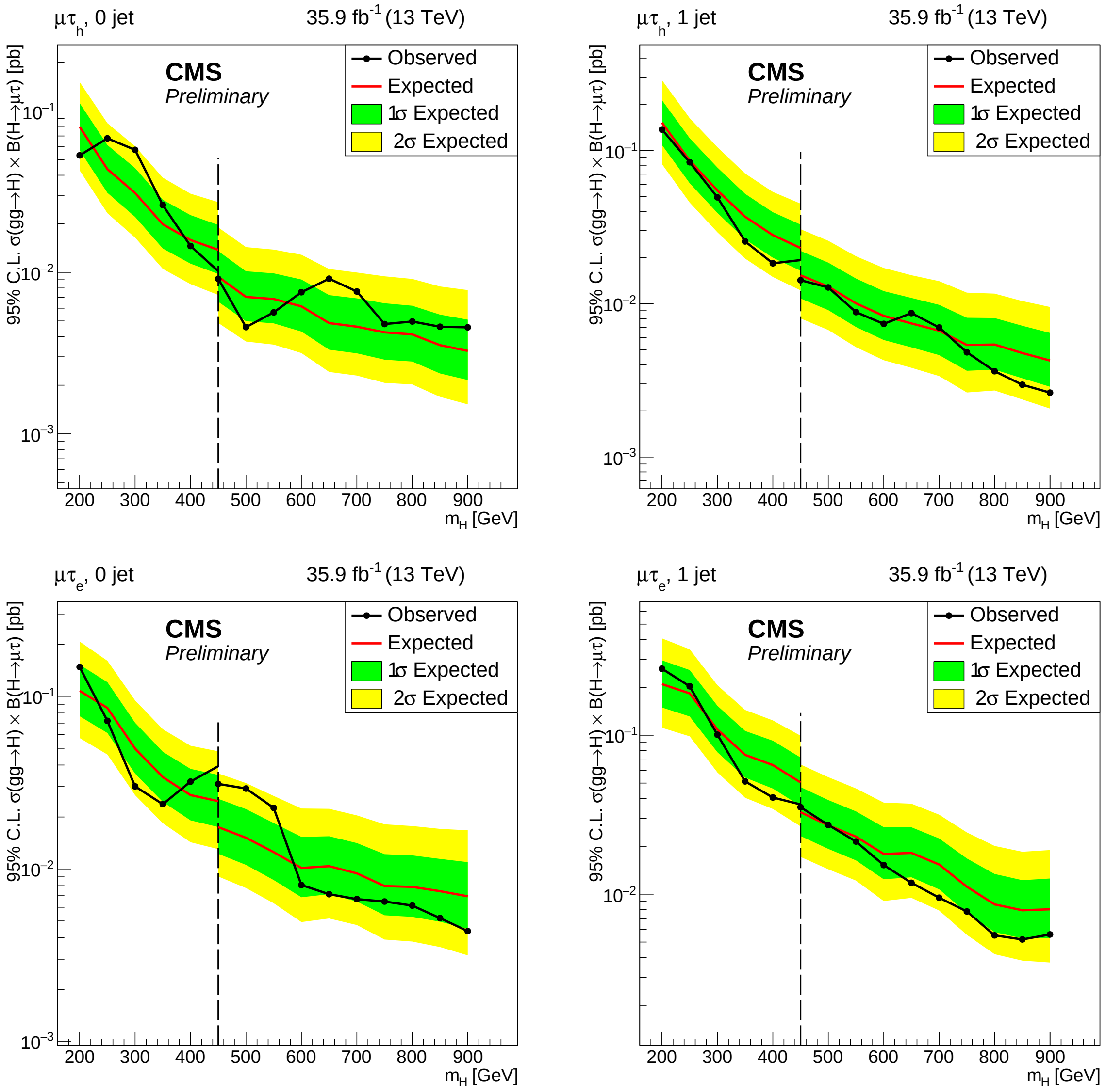

Figure 4: The observed and median expected 95% limits on $\sigma(gg \to \mathrm{H}) \times B(\mathrm{H} \to \mu\tau)$, for the $\mu\tau_h$ (top) and $\mu\tau_e$ (bottom) channels, for 0-jet (left) and 1-jet (right) categories.

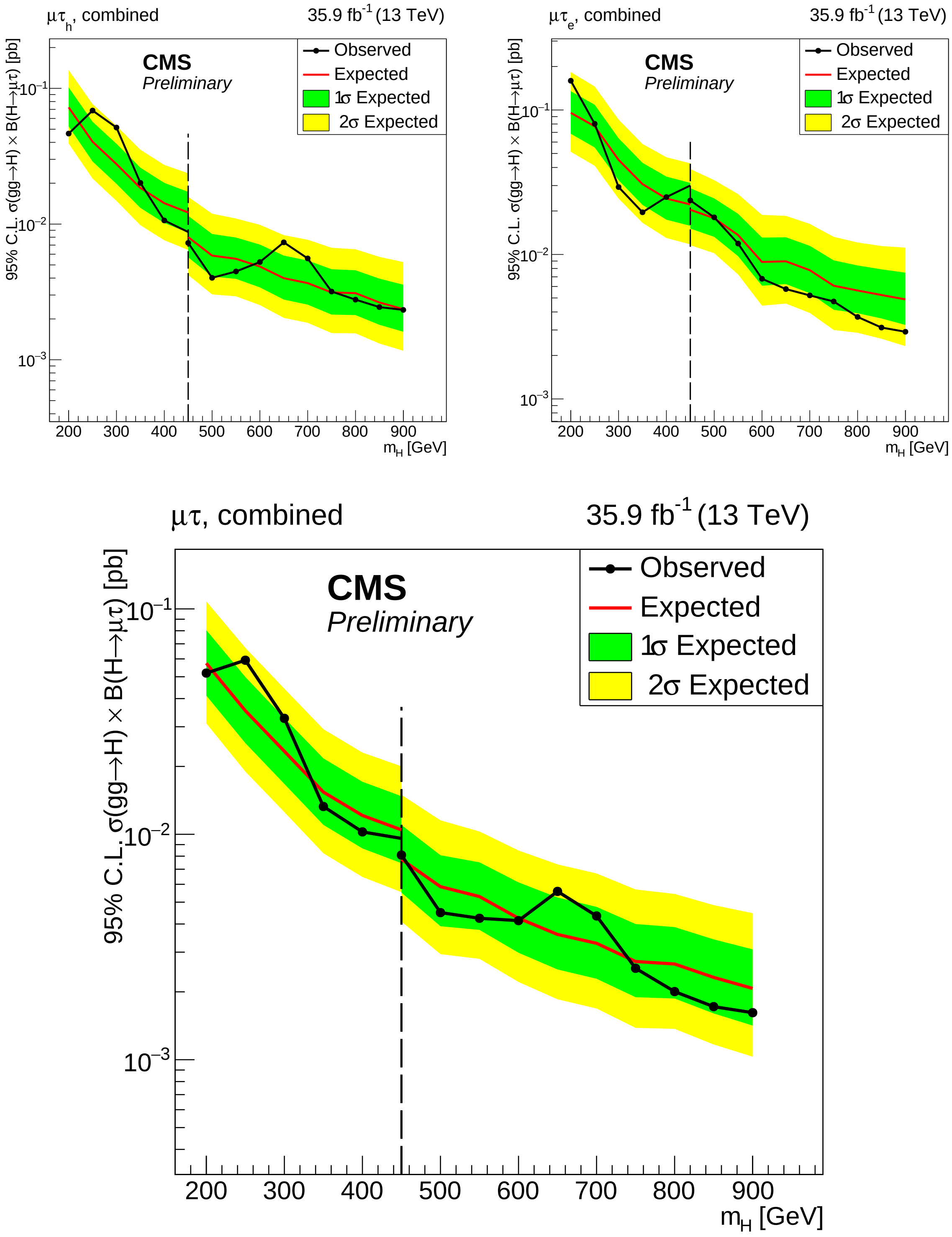

Figure 5: The combined observed and median expected 95% limits on $\sigma(gg \to \mathrm{H}) \times B(\mathrm{H} \to \mu\tau)$, for $\mu\tau_h$ (top left) and $\mu\tau_\mathrm{e}$ (top right) channels, and their combination $\mu\tau$ (bottom)

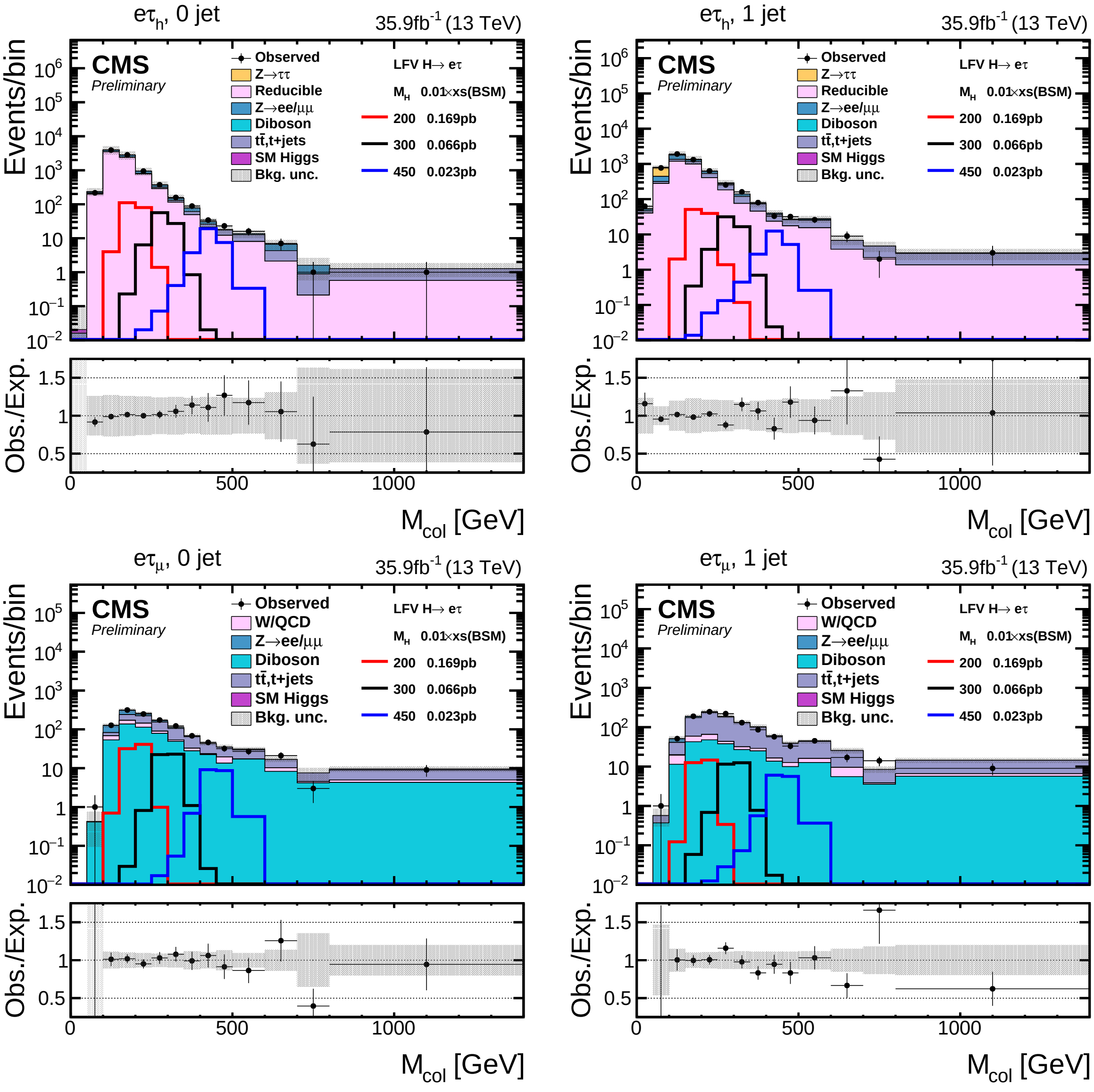

Figure 6: The M_{col} distribution in the signal region, for the eτ_h (top) and eτ_μ (bottom) channels for the Higgs mass in the range 200-450 GeV for 0-jet (left) and 1-jet (right) categories.

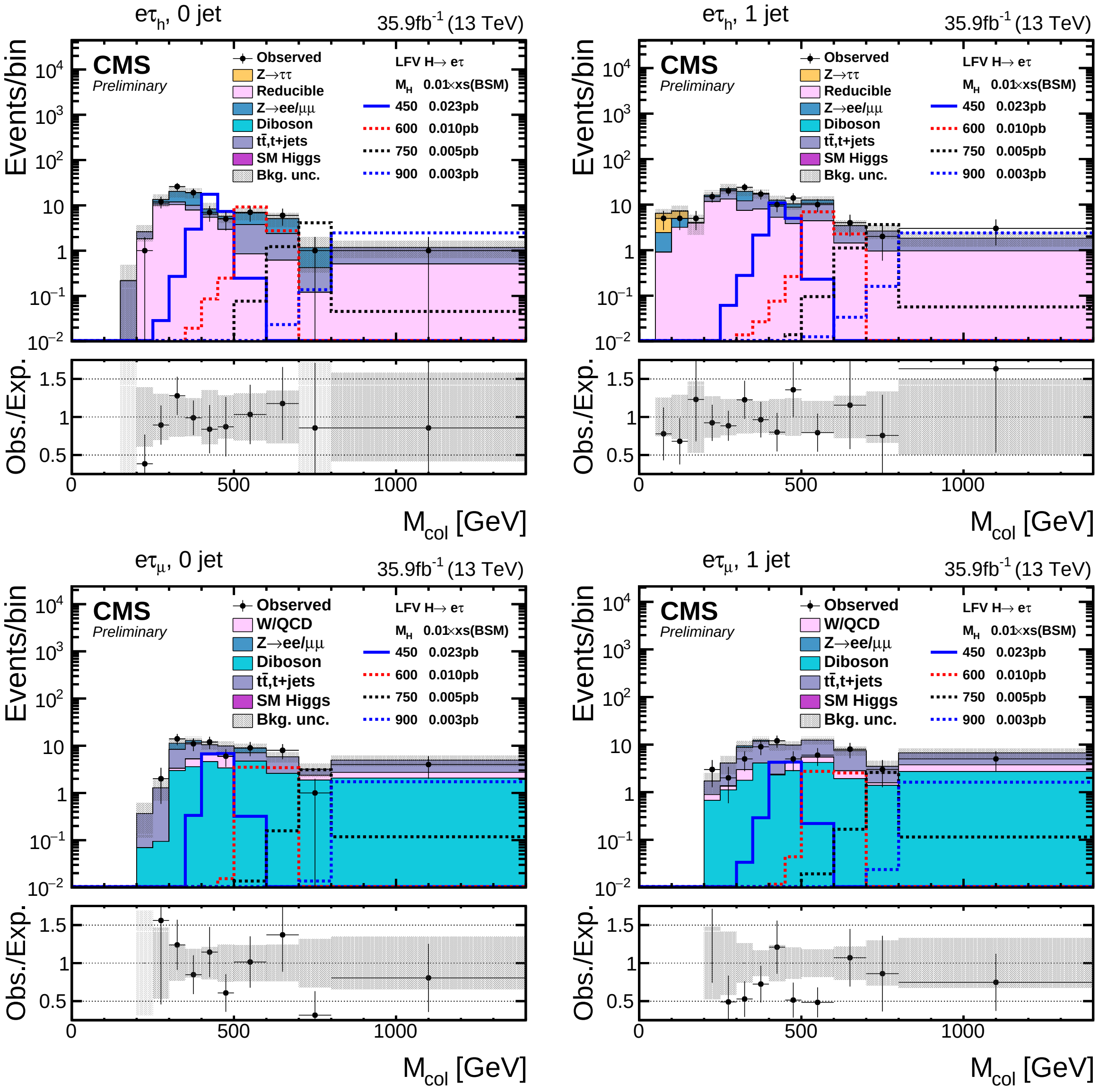

Figure 7: The $M_{\rm col}$ distribution in the signal region, for the $e\tau_h$ (top) and $e\tau_\mu$ (bottom) channels for the Higgs mass in the range 450-900 GeV for 0-jet (left) and 1-jet (right) categories.

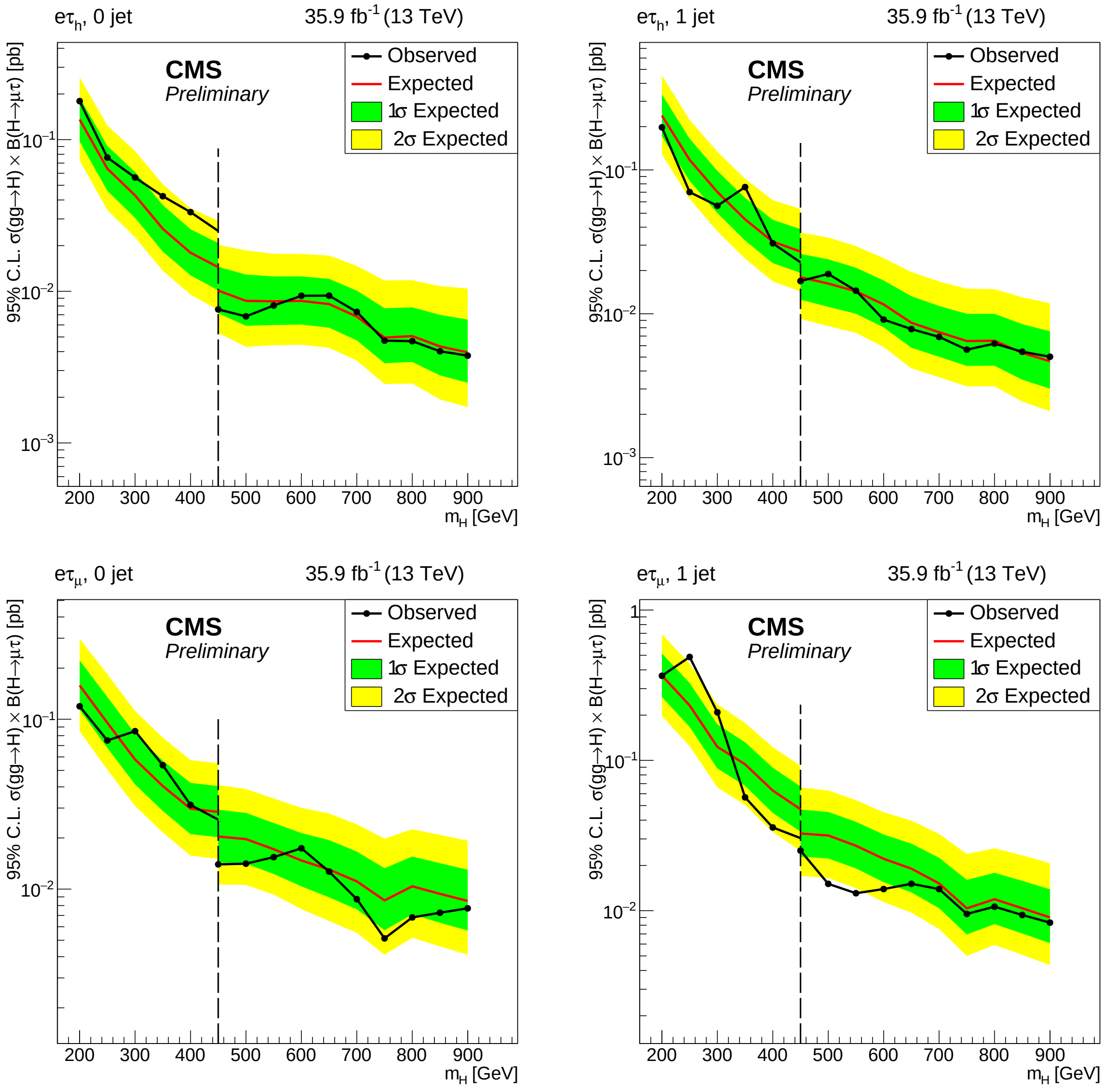

Figure 8: The observed and median expected 95% limits on $\sigma(gg \to \mathrm{H}) \times B(\mathrm{H} \to \mathrm{e}\tau)$, for the $\mathrm{e}\tau_h$ (top) and $\mathrm{e}\tau_\mu$ (bottom) channels, for 0-jet (left) and 1-jet (right) categories.

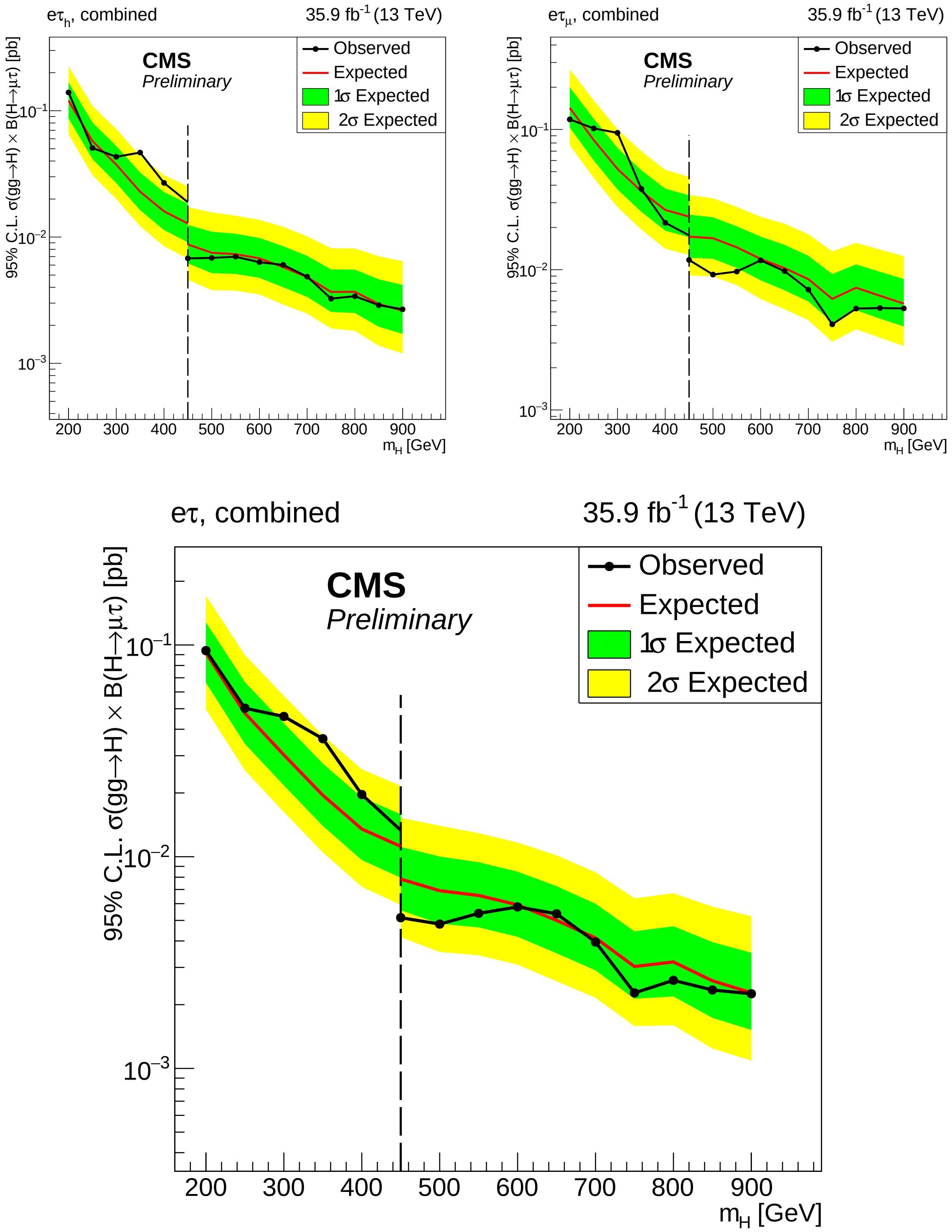

Figure 9: The combined observed and median expected 95% limits on $\sigma(gg \to \mathrm{H}) \times B(\mathrm{H} \to \mathrm{e}\tau)$, for $\mathrm{e}\tau_h$ (top left) and $\mathrm{e}\tau_\mu$ (top right) channels, and their combination $\mathrm{e}\tau$ (bottom).

References

[1] ATLAS Collaboration, "Observation of a new particle in the search for the Standard Model Higgs boson with the ATLAS detector at the LHC", *Phys. Lett. B* **716** (2012) 1, `doi:10.1016/j.physletb.2012.08.020`, `arXiv:1207.7214`.

[2] CMS Collaboration, "Observation of a new boson at a mass of 125 GeV with the CMS experiment at the LHC", *Phys. Lett. B* **716** (2012) 30, `doi:10.1016/j.physletb.2012.08.021`, `arXiv:1207.7235`.

[3] CMS Collaboration, "Observation of a new boson with mass near 125 GeV in pp collisions at $\sqrt{s} = 7$ and 8 TeV", *JHEP* **06** (2013) 081, `doi:10.1007/JHEP06(2013)081`, `arXiv:1303.4571`.

[4] F. Englert and R. Brout, "Broken Symmetry and the Mass of Gauge Vector Mesons", *Phys. Rev. Lett.* **13** (1964) 321, `doi:10.1103/PhysRevLett.13.321`.

[5] P. W. Higgs, "Broken symmetries, massless particles and gauge fields", *Phys. Lett.* **12** (1964) 132, `doi:10.1016/0031-9163(64)91136-9`.

[6] P. W. Higgs, "Broken Symmetries and the Masses of Gauge Bosons", *Phys. Rev. Lett.* **13** (1964) 508, `doi:10.1103/PhysRevLett.13.508`.

[7] G. S. Guralnik, C. R. Hagen, and T. W. B. Kibble, "Global Conservation Laws and Massless Particles", *Phys. Rev. Lett.* **13** (1964) 585, `doi:10.1103/PhysRevLett.13.585`.

[8] P. W. Higgs, "Spontaneous Symmetry Breakdown without Massless Bosons", *Phys. Rev.* **145** (1966) 1156, `doi:10.1103/PhysRev.145.1156`.

[9] T. W. B. Kibble, "Symmetry Breaking in Non-Abelian Gauge Theories", *Phys. Rev.* **155** (1967) 1554, `doi:10.1103/PhysRev.155.1554`.

[10] ATLAS Collaboration and CMS Collaboration, "Measurements of the Higgs boson production and decay rates and constraints on its couplings from a combined ATLAS and CMS analysis of the LHC pp collision data at $\sqrt{s} = 7$ and 8 TeV", *JHEP* **08** (2016) 045, `doi:10.1007/JHEP08(2016)045`, `arXiv:1606.02266`.

[11] CMS Collaboration, "Combined measurements of higgs boson couplings in proton-proton collisions at $\sqrt{s} = 13$ tev", (2019). `arXiv:1809.10733`. Submitted to EPJC.

[12] J. D. Bjorken and S. Weinberg, "Mechanism for Nonconservation of Muon Number", *Phys. Rev. Lett.* **38** (1977) 622, `doi:10.1103/PhysRevLett.38.622`.

[13] J. L. Diaz-Cruz and J. J. Toscano, "Lepton flavor violating decays of Higgs bosons beyond the standard model", *Phys. Rev. D* **62** (2000) 116005, `doi:10.1103/PhysRevD.62.116005`, `arXiv:hep-ph/9910233`.

[14] T. Han and D. Marfatia, "$h \to \mu\tau$ at hadron colliders", *Phys. Rev. Lett.* **86** (2001) 1442, `doi:10.1103/PhysRevLett.86.1442`, `arXiv:hep-ph/0008141`.

[15] E. Arganda, A. M. Curiel, M. J. Herrero, and D. Temes, "Lepton flavor violating Higgs boson decays from massive seesaw neutrinos", *Phys. Rev. D* **71** (2005) 035011, `doi:10.1103/PhysRevD.71.035011`, `arXiv:hep-ph/0407302`.

[16] A. Arhrib, Y. Cheng, and O. C. W. Kong, "Comprehensive analysis on lepton flavor violating Higgs boson to $\mu^{\mp}\tau^{\pm}$ decay in supersymmetry without R parity", *Phys. Rev. D* **87** (2013) 015025, `doi:10.1103/PhysRevD.87.015025`, `arXiv:1210.8241`.

[17] M. Arana-Catania, E. Arganda, and M. J. Herrero, "Non-decoupling SUSY in LFV Higgs decays: a window to new physics at the LHC", *JHEP* **09** (2013) 160, `doi:10.1007/JHEP09(2013)160`, `arXiv:1304.3371`. [Erratum: `doi:10.1007/JHEP10(2015)192`].

[18] E. Arganda, M. J. Herrero, R. Morales, and A. Szynkman, "Analysis of the $h, H, A \to \tau\mu$ decays induced from SUSY loops within the Mass Insertion Approximation", *JHEP* **03** (2016) 055, `doi:10.1007/JHEP03(2016)055`, `arXiv:1510.04685`.

[19] E. Arganda, M. J. Herrero, X. Marcano, and C. Weiland, "Enhancement of the lepton flavor violating Higgs boson decay rates from SUSY loops in the inverse seesaw model", *Phys. Rev. D* **93** (2016) 055010, `doi:10.1103/PhysRevD.93.055010`, `arXiv:1508.04623`.

[20] K. Agashe and R. Contino, "Composite Higgs-mediated flavor-changing neutral current", *Phys. Rev. D* **80** (2009) 075016, `doi:10.1103/PhysRevD.80.075016`, `arXiv:0906.1542`.

[21] A. Azatov, M. Toharia, and L. Zhu, "Higgs mediated flavor changing neutral currents in warped extra dimensions", *Phys. Rev. D* **80** (2009) 035016, `doi:10.1103/PhysRevD.80.035016`, `arXiv:0906.1990`.

[22] H. Ishimori et al., "Non-Abelian Discrete Symmetries in Particle Physics", *Prog. Theor. Phys. Suppl.* **183** (2010) 1, `doi:10.1143/PTPS.183.1`, `arXiv:1003.3552`.

[23] G. Perez and L. Randall, "Natural neutrino masses and mixings from warped geometry", *JHEP* **01** (2009) 077, `doi:10.1088/1126-6708/2009/01/077`, `arXiv:0805.4652`.

[24] S. Casagrande et al., "Flavor physics in the Randall-Sundrum model I. Theoretical setup and electroweak precision tests", *JHEP* **10** (2008) 094, `doi:10.1088/1126-6708/2008/10/094`, `arXiv:0807.4937`.

[25] A. J. Buras, B. Duling, and S. Gori, "The impact of Kaluza-Klein fermions on Standard Model fermion couplings in a RS model with custodial protection", *JHEP* **09** (2009) 076, `doi:10.1088/1126-6708/2009/09/076`, `arXiv:0905.2318`.

[26] M. Blanke et al., "$\Delta F = 2$ observables and fine-tuning in a warped extra dimension with custodial protection ", *JHEP* **03** (2009) 001, `doi:10.1088/1126-6708/2009/03/001`, `arXiv:0809.1073`.

[27] G. F. Giudice and O. Lebedev, "Higgs-dependent Yukawa couplings", *Phys. Lett. B* **665** (2008) 79, `doi:10.1016/j.physletb.2008.05.062`, `arXiv:0804.1753`.

[28] J. A. Aguilar-Saavedra, "A minimal set of top-Higgs anomalous couplings", *Nucl. Phys. B* **821** (2009) 215, `doi:10.1016/j.nuclphysb.2009.06.022`, `arXiv:0904.2387`.

[29] M. E. Albrecht et al., "Electroweak and flavour structure of a warped extra dimension with custodial protection", *JHEP* **09** (2009) 064, `doi:10.1088/1126-6708/2009/09/064`, `arXiv:0903.2415`.

[30] A. Goudelis, O. Lebedev, and J. H. Park, "Higgs-induced lepton flavor violation", *Phys. Lett. B* **707** (2012) 369, `doi:10.1016/j.physletb.2011.12.059`, `arXiv:1111.1715`.

[31] D. McKeen, M. Pospelov, and A. Ritz, "Modified Higgs branching ratios versus CP and lepton flavor violation", *Phys. Rev. D* **86** (2012) 113004, `doi:10.1103/PhysRevD.86.113004`, `arXiv:1208.4597`.

[32] A. Pilaftsis, "Lepton flavour nonconservation in H^0 decays", *Phys. Lett. B* **285** (1992) 68, `doi:10.1016/0370-2693(92)91301-O`.

[33] J. G. Körner, A. Pilaftsis, and K. Schilcher, "Leptonic CP asymmetries in flavor-changing H^0 decays", *Phys. Rev. D* **47** (1993) 1080, `doi:10.1103/PhysRevD.47.1080`.

[34] E. Arganda, M. J. Herrero, X. Marcano, and C. Weiland, "Imprints of massive inverse seesaw model neutrinos in lepton flavor violating Higgs boson decays", *Phys. Rev. D* **91** (2015) 015001, `doi:10.1103/PhysRevD.91.015001`, `arXiv:1405.4300`.

[35] M. Sher and K. Thrasher, "Flavor-changing leptonic decays of heavy Higgs bosons", *Phys. Rev. D* **93** (2016) 055021, `doi:10.1103/PhysRevD.93.055021`.

[36] A. M. Sirunyan et al., "Search for lepton flavour violating decays of the Higgs boson to $\mu\tau$ and $e\tau$ in proton-proton collisions at $\sqrt{s} = 13$ TeV", *JHEP* **06** (2018) 001, `doi:10.1007/JHEP06(2018)001`, `arXiv:1712.07173`.

[37] CMS Collaboration, "Search for lepton-flavour-violating decays of the Higgs boson", *Phys. Lett. B* **749** (2015) 337, `doi:10.1016/j.physletb.2015.07.053`, `arXiv:1502.07400`.

[38] CMS Collaboration, "Search for lepton flavour violating decays of the Higgs boson to $e\tau$ and $e\mu$ in proton-proton collisions at $\sqrt{s}$=8 TeV", *Phys. Lett. B* **763** (2016) 472, `doi:10.1016/j.physletb.2016.09.062`, `arXiv:1607.03561`.

[39] ATLAS Collaboration, "Search for lepton-flavour-violating decays of the Higgs and Z bosons with the ATLAS detector", *Eur. Phys. J. C* **77** (2017) 70, `doi:10.1140/epjc/s10052-017-4624-0`, `arXiv:1604.07730`.

[40] ATLAS Collaboration, "Search for lepton-flavour-violating $H \to \mu\tau$ decays of the Higgs boson with the ATLAS detector", *JHEP* **11** (2015) 211, `doi:10.1007/JHEP11(2015)211`, `arXiv:1508.03372`.

[41] M. Buschmann, J. Kopp, J. Liu, and X.-P. Wang, "New signatures of flavor violating Higgs couplings", *JHEP* **06** (2016) 149, `doi:10.1007/JHEP06(2016)149`, `arXiv:1601.02616`.

[42] CMS Collaboration, "Evidence for the direct decay of the 125 GeV Higgs boson to fermions", *Nature Phys.* **10** (2014) 557, `doi:10.1038/nphys3005`, `arXiv:1401.6527`.

[43] CMS Collaboration, "Evidence for the 125 GeV Higgs boson decaying to a pair of τ leptons", *JHEP* **05** (2014) 104, `doi:10.1007/JHEP05(2014)104`, `arXiv:1401.5041`.

[44] CMS Collaboration, "Observation of the Higgs boson decay to a pair of τ leptons with the CMS detector", *Phys. Lett. B* **779** (2018) 283, `doi:10.1016/j.physletb.2018.02.004`, `arXiv:1708.00373`.

[45] CMS Collaboration, "Search for additional neutral MSSM Higgs bosons in the $\tau\tau$ final state in proton-proton collisions at $\sqrt{s}$ =13 TeV", *JHEP* **7** (2018) 007, `doi:10.1007/JHEP09(2018)007`, `arXiv:1408.3316`.

[46] ATLAS Collaboration, "Evidence for the Higgs-boson Yukawa coupling to tau leptons with the ATLAS detector", *JHEP* **04** (2015) 117, `doi:10.1007/JHEP04(2015)117`, `arXiv:1501.04943`.

[47] CMS Collaboration, "The CMS experiment at the CERN LHC", *JINST* **3** (2008) S08004, `doi:10.1088/1748-0221/3/08/S08004`.

[48] P. Nason, "A new method for combining NLO QCD with shower Monte Carlo algorithms", *JHEP* **11** (2004) 040, `doi:10.1088/1126-6708/2004/11/040`, `arXiv:hep-ph/0409146`.

[49] S. Frixione, P. Nason, and C. Oleari, "Matching NLO QCD computations with parton shower simulations: the POWHEG method", *JHEP* **11** (2007) 070, `doi:10.1088/1126-6708/2007/11/070`, `arXiv:0709.2092`.

[50] S. Alioli, P. Nason, C. Oleari, and E. Re, "A general framework for implementing NLO calculations in shower Monte Carlo programs: the POWHEG BOX", *JHEP* **06** (2010) 043, `doi:10.1007/JHEP06(2010)043`, `arXiv:1002.2581`.

[51] S. Alioli et al., "Jet pair production in POWHEG", *JHEP* **04** (2011) 081, `doi:10.1007/JHEP04(2011)081`, `arXiv:1012.3380`.

[52] S. Alioli, P. Nason, C. Oleari, and E. Re, "NLO Higgs boson production via gluon fusion matched with shower in POWHEG", *JHEP* **04** (2009) 002, `doi:10.1088/1126-6708/2009/04/002`, `arXiv:0812.0578`.

[53] E. Bagnaschi, G. Degrassi, P. Slavich, and A. Vicini, "Higgs production via gluon fusion in the POWHEG approach in the SM and in the MSSM", *JHEP* **02** (2012) 088, `doi:10.1007/JHEP02(2012)088`, `arXiv:1111.2854`.

[54] H. M. Georgi, S. L. Glashow, M. E. Machacek, and D. V. Nanopoulos, "Higgs Bosons from Two-Gluon Annihilation in Proton Proton Collisions", *Phys. Rev. Lett.* **40** (1978) 692, `doi:10.1103/PhysRevLett.40.692`.

[55] J. Alwall et al., "The automated computation of tree-level and next-to-leading order differential cross sections, and their matching to parton shower simulations", *JHEP* **07** (2014) 079, `doi:10.1007/JHEP07(2014)079`, `arXiv:1405.0301`.

[56] J. Alwall et al., "Comparative study of various algorithms for the merging of parton showers and matrix elements in hadronic collisions", *Eur. Phys. J. C* **53** (2008) 473, `doi:10.1140/epjc/s10052-007-0490-5`, `arXiv:0706.2569`.

[57] R. Frederix and S. Frixione, "Merging meets matching in MC@NLO", *JHEP* **12** (2012) 061, `doi:10.1007/JHEP12(2012)061`, `arXiv:1209.6215`.

[58] T. Sjöstrand et al., "An introduction to PYTHIA 8.2", *Comput. Phys. Commun.* **191** (2015) 159, `doi:10.1016/j.cpc.2015.01.024`, `arXiv:1410.3012`.

[59] CMS Collaboration, "Event generator tunes obtained from underlying event and multiparton scattering measurements", *Eur. Phys. J. C* **76** (2016) 155, `doi:10.1140/epjc/s10052-016-3988-x`, `arXiv:1512.00815`.

[60] GEANT4 Collaboration, "GEANT4 — a simulation toolkit", *Nucl. Instrum. Meth. A* **506** (2003) 250, `doi:10.1016/S0168-9002(03)01368-8`.

[61] CMS Collaboration, "Particle-flow reconstruction and global event description with the CMS detector", *JINST* **12** (2017) P10003, `doi:10.1088/1748-0221/12/10/P10003`, `arXiv:1706.04965`.

[62] M. Cacciari, G. P. Salam, and G. Soyez, "The anti-k_t jet clustering algorithm", *JHEP* **04** (2008) 063, `doi:10.1088/1126-6708/2008/04/063`, `arXiv:0802.1189`.

[63] M. Cacciari, G. P. Salam, and G. Soyez, "FastJet user manual", *Eur. Phys. J. C* **72** (2012) 1896, `doi:10.1140/epjc/s10052-012-1896-2`, `arXiv:1111.6097`.

[64] CMS Collaboration, "Performance of the CMS muon detector and muon reconstruction with proton proton collisions at $\sqrt{s} = 13$ TeV", *JINST* **13** (2018) P06015, `doi:10.1088/1748-0221/13/06/p06015`, `arXiv:1804.04528v2`.

[65] CMS Collaboration, "Performance of electron reconstruction and selection with the CMS detector in proton-proton collisions at $\sqrt{s}$ = 8 TeV", *JINST* **10** (2015) P06005, `doi:10.1088/1748-0221/10/06/P06005`, `arXiv:1502.02701`.

[66] M. Cacciari, G. P. Salam, "Dispelling the N^3 myth for the k_t jet-finder", *Phys. Lett. B* **641** (2006) 57, `doi:10.1016/j.physletb.2006.08.037`, `arXiv:hep-ph/0512210`.

[67] CMS Collaboration, "Determination of jet energy calibration and transverse momentum resolution in CMS", *JINST* **6** (2011) 11002, `doi:10.1088/1748-0221/6/11/P11002`, `arXiv:1107.4277`.

[68] CMS Collaboration, "Jet energy scale and resolution in the CMS experiment in pp collisions at 8 TeV", *JINST* **12** (2017) P02014, `doi:10.1088/1748-0221/12/02/P02014`, `arXiv:1607.03663`.

[69] CMS Collaboration, "Reconstruction and identification of τ lepton decays to hadrons and ν_τ at CMS", *JINST* **11** (2016) P01019, `doi:10.1088/1748-0221/11/01/P01019`, `arXiv:1510.07488`.

[70] CMS Collaboration, "Performance of reconstruction and identification of τ leptons decaying to hadrons and ν_τ in pp collisions at $\sqrt{s}$ = 13 TeV", *JINST* **13** (2018) P10005, `doi:10.1088/1748-0221/13/10/p10005`, `arXiv:1809.02816`.

[71] M. Cacciari, G. P. Salam, and G. Soyez, "The catchment area of jets", *JHEP* **04** (2008) 005, `doi:10.1088/1126-6708/2008/04/005`, `arXiv:0802.1188`.

[72] M. Cacciari and G. P. Salam, "Pileup subtraction using jet areas", *Phys. Lett. B* **659** (2008) 119, `doi:10.1016/j.physletb.2007.09.077`, `arXiv:0707.1378`.

[73] CMS Collaboration, "Performance of the CMS missing transverse momentum reconstruction in pp data at $\sqrt{s}$ = 8 TeV", *JINST* **10** (2015) P02006, `doi:10.1088/1748-0221/10/02/P02006`, `arXiv:1411.0511`.

[74] R. K. Ellis, I. Hinchliffe, M. Soldate, and J. J. Van Der Bij, "Higgs Decay to $\tau^+\tau^-$: A possible signature of intermediate mass Higgs bosons at high energy hadron colliders", *Nucl. Phys. B* **297** (1988) 221, `doi:10.1016/0550-3213(88)90019-3`.

[75] CMS Collaboration, “Identification of heavy-flavour jets with the CMS detector in pp collisions at $\sqrt{s} = 13$ TeV”, *JINST* **13** (2018) P05011, `doi:10.1088/1748-0221/13/05/P05011`, `arXiv:1712.07158`.

[76] LHC Higgs Cross Section Working Group Collaboration, “Handbook of LHC Higgs Cross Sections: 4. Deciphering the Nature of the Higgs Sector”, `arXiv:1610.07922`.

[77] ATLAS and CMS Collaborations, LHC Higgs Combination Group, “Procedure for the LHC Higgs boson search combination in Summer 2011”, Technical Report ATL-PHYS-PUB 2011-11, CMS NOTE 2011/005, 2011.

[78] T. Junk, “Confidence level computation for combining searches with small statistics”, *Nucl. Instrum. Meth. A* **434** (1999) 435, `doi:10.1016/S0168-9002(99)00498-2`, `arXiv:hep-ex/9902006`.

[79] A. L. Read, “Presentation of search results: the CL_s technique”, *J. Phys. G* **28** (2002) 2693, `doi:10.1088/0954-3899/28/10/313`.